J Mater Sci (2018) 53:16511–16523

Energy materials

Solvent-controlled morphology of bismuth sulfide for supercapacitor applications

Ewa Miniach[1] and Grażyna Gryglewicz[1,*]

[1] *Department of Polymer and Carbonaceous Materials, Faculty of Chemistry, Wrocław University of Technology, Gdańska 7/9, 50-344 Wrocław, Poland*

Received: 4 June 2018
Accepted: 10 August 2018
Published online: 17 August 2018

ABSTRACT

In our study, we report a facile solvothermal method for the synthesis of Bi_2S_3 nanoparticles with unique morphologies using water and mixed solvent systems, such as ethylene glycol/water (1:1, v/v) and butyldiglycol/water (1:1, v/v). Altering the solution mixtures used in the solvothermal synthesis allowed the shape of the Bi_2S_3 nanoparticles to be controlled. The synthesis of Bi_2S_3 in water at 150 °C for 24 h led to the formation of sphere-like particles 100–300 nm in size. Very uniform spherical nanospheres with diameters from 50 to 90 nm formed when ethylene glycol/water mixture (1:1, v/v) was used as the solvent under the same solvothermal conditions. The butyldiglycol/water mixture promoted the formation of plate-shaped Bi_2S_3 nanoparticles composed of nanorods. The electrochemical properties of the Bi_2S_3 samples were determined in a three-electrode cell in 6 mol L^{-1} KOH using cyclic voltammetry, galvanostatic charging/discharging and impedance spectroscopy. Among the synthesized materials, the Bi_2S_3 sample obtained in the butyldiglycol/water mixture exhibited a superior capacitive behavior with an outstanding capacitance of 550 F g^{-1} (at 0.5 A g^{-1}), and great cycle stability, which was reflected by a capacitance retention of 87% after 500 charge/discharge cycles. These results demonstrate the high potential of Bi_2S_3 as an active electrode material for supercapacitors.

Introduction

Electrochemical energy storage systems include supercapacitors, batteries and fuel cells. Supercapacitors have advantages over well-known electrochemical storage devices, such as large power capability and long cycle life (up to 10^6 cycles) [1, 2]. Despite their exceptional ability to withstand and produce high currents, supercapacitors exhibit relatively low energy densities, which are proportional to the capacitance (*C*, expressed in Farads) and potential difference (*V*, given in Volts), as shown in the following equation:

Address correspondence to E-mail: grazyna.gryglewicz@pwr.edu.pl

https://doi.org/10.1007/s10853-018-2785-3

$$E = \frac{1}{2}CV^2. \quad (1)$$

In addition to poor energy density, supercapacitor technology has another issue that should be addressed. The majority of commercial supercapacitors work in expensive and flammable organic media, such as $TEABF_4$ dissolved in acetonitrile, resulting in high manufacturing costs and reduced operational safety [3]. The currently fast-growing technology of aqueous-based supercapacitors that operate in low-cost and environmentally friendly electrolytes is a key approach to further develop devices with improved energy densities.

The operational parameters of supercapacitors, including their power and energy density, are dependent on the applied electrode; therefore, there is now a great deal of interest in the development of electrode materials that provide high capacitance values and can work in wide potential windows [3]. Despite the excellent power capability and high electrochemical stability of the classical activated carbon electrodes widely used for commercial applications, they still exhibit relatively low specific capacitances, not exceeding 200 F g^{-1}, while operating in aqueous electrolytes [4]. Over the past two decades, many studies have been conducted on both the synthesis and application of transition metal oxides, such as MnO_2 [5–8], NiO [9], Co_3O_4 [10, 11], Fe_2O_3 [12, 13] and Fe_3O_4 [14], as electrodes for supercapacitors. The pseudocapacitive charge storage mechanism of oxides is different from the mechanism based on electrical double layer (EDL) formation at the carbon electrode–electrolyte interface, which enables distinctly higher capacitance values due to fast and reversible redox reactions [15].

Recently, metal sulfides, which have slightly higher electrical conductivities than metal oxides, have been shown to be promising candidates for electrochemically active materials in lithium-ion batteries (LIB) and supercapacitors [16–18]. One metal sulfide, Bi_2S_3, is a layer-structured semiconductor, which crystallizes in an orthorhombic system. This metal sulfide has attracted scientific interest for a broad range of applications, including electronic and optoelectronic devices [19], photocatalysis [20–22] and hydrogen storage [23, 24]. Recently, the unique pseudocapacitive behavior of Bi_2S_3, which was reported by Nie et al. [25], has attracted more attention, and the metal sulfide has been studied as a supercapacitor electrode material [20–22, 24–32] due to its remarkable specific capacitance reaching up to 400 F g^{-1} [33].

The key to further progress in electrode material design is to establish the effect of different properties, such as the nanoparticle size and morphology of synthesized metal sulfides, on the electrochemical performance. Therefore, attempts have been made to develop an easily replicated and morphology-controlled synthesis method for Bi_2S_3. Thus far, the most commonly reported Bi_2S_3 structures are nanorods [20, 23, 25, 28, 34–36] and more complex architectures, such as nanoflowers [24, 27, 29, 32] or nanospheres [37], composed of nanorod-like units. All of these structures have been obtained using various approaches, including solvothermal syntheses [21, 22, 27, 28, 30, 34, 38]. The nanostructure of Bi_2S_3 is highly sensitive to synthesis parameters such as the substrate molar ratio [27, 34], temperature [22, 34, 39], synthesis time [34] and sulfur precursor [38, 39]. However, optimizing the solvothermal process by altering the solvent mixture has not attracted much attention. According to previous reports [39, 40], syntheses in mixed solvents favor the formation of nanostructures with more uniform sizes and uncommon architectures compared with syntheses in single solvents. Most reports have focused on the synthesis of Bi_2S_3 in water [19, 22, 23, 25, 27, 34, 38, 41]. The usage of other solvents, including ethanol [21], ethylene glycol [20] or glycerol [36], has been rarely reported.

In this study, we proposed a morphology-controlled synthesis of Bi_2S_3 nanostructures by a solvothermal approach with different solvent mixtures, such as ethylene glycol/water (1:1, v/v) and a novel butyldiglycol/water (1:1, v/v) system. Butyldiglycol, also known as diethylene glycol butyl ether, is an inexpensive solvent that is easily miscible with water and used in many commercial products. Despite its interesting surfactant-like properties, butyldiglycol has not yet been used in the synthesis of metal sulfides. The morphological–electrochemical property dependence of the Bi_2S_3 electrodes was evaluated in a three-electrode cell operating in a wide potential window between − 0.1 and − 0.9 V. The Bi_2S_3 nanorods synthesized in the butyldiglycol/water (1:1, v/v) mixture exhibited the best electrochemical performance, as reflected by their outstanding specific capacitance of 550 F g^{-1} at 0.5 A g^{-1}. This is the first time such a high

capacitance value has been demonstrated for a Bi_2S_3 electrode.

Materials and methods

Synthesis of Bi_2S_3

The synthesis of Bi_2S_3 with different morphologies was performed in a stainless steel autoclave (250 mL) using a solvothermal approach. The precursors of the bismuth and sulfur ions, namely, bismuth nitrate pentahydrate (Sigma-Aldrich, ACS reagent, ≥ 99.0%) and thioacetamide C_2H_5NS (TAA) (Sigma-Aldrich, ACS reagent, ≥ 98.0%), were used in a molar ratio of 1:1. The mass ratio of bismuth salt to thioacetamide was equal to 6.5:1. Briefly, the experimental procedure was as follows. First, 100 mL of solvent [Milli-Q water/ethylene glycol (EG)/butyldiglycol (BG)] was mixed with an aqueous solution of $Bi(NO_3)_3{\cdot}5\ H_2O$ (0.30 g; 70 mL). Subsequently, TAA, which was dissolved in water (30 mL), was added dropwise under vigorous stirring. The as-prepared reaction mixture was transferred to an autoclave and heated at 150 °C for 24 h. Finally, the obtained samples were centrifuged, washed with Milli-Q water and isopropanol, and dried in a vacuum oven at 60 °C for 24 h. The samples synthesized in water and the ethylene glycol/water (1:1, v/v) and butyldiglycol/water (1:1, v/v) mixtures were labeled Bi_2S_3-W, Bi_2S_3-EG/W and Bi_2S_3-BG/W, respectively.

Material characterization

The structure of the obtained materials was determined using the X-ray diffraction (XRD) spectra recorded on an Ultima IV Rigaku analyzer using CuKα radiation (λ = 1.54056 Å) at 40 kV and 30 mA. To determine the surface elemental composition and valence states of Bi and S in the products, X-ray photoelectron spectroscopy (XPS) analyses were performed using a PHI 5000 VersaProbe instrument. Field emission scanning electron microscopy (FESEM) and high-resolution transmission microscopy (HRTEM) micrographs were acquired with a Merlin Zeiss field emission scanning electron microscope operating at an accelerating voltage of 3 kV and a FEI TITAN^3 G2 60-300 microscope, respectively. The porous structure of the products was determined by nitrogen adsorption at 77 K on an Autosorb IQ gas sorption analyzer (Quantachrome). The specific surface area and pore size distribution of the Bi_2S_3 samples were evaluated applying the Brunauer–Emmett–Teller (BET) and quenched solid-state functional theory (QSDFT) methods, respectively. The total pore volume (V_T) was calculated from the adsorption isotherms at p/p_o = 0.96. The Dubinin–Radushkevich equation was used to assess the micropore volume (V_{mic}). The mesopore volume (V_{mes}) was evaluated as the difference between V_T and V_{mic}.

Electrochemical measurements

The electrochemical performance of the tested electrodes was evaluated in a three-electrode configuration in a 6 mol L^{-1} KOH aqueous electrolyte using cyclic voltammetry (CV) and galvanostatic charge–discharge (GCD) measurements with a VMP3 Biologic potentiostat/galvanostat (France). The electrochemical impedance spectroscopy (EIS) investigation was carried out at the open-circuit potential in the frequency range from 100 kHz to 10 mHz. The Bi_2S_3-based pellets obtained by mixing the electroactive material, polyvinylidene fluoride (PVDF) and acetylene black at a mass ratio of 75:10:15 were used as the working electrodes, and activated carbon (AC) and Hg/HgO were the counter and reference electrodes, respectively. The AC pellet consisted of 85% active material (KOH-activated carbon from mesophase pitch-based semi-coke), 10% PVDF and 5% acetylene black. The pellet preparation included mixing the active material, percolator and binder in acetone, pressing the as-obtained homogenous slurry at a pressure of 18 MPa and drying the slurry at 110 °C for 1 h. To eliminate the influence of the mass on the capacitance, the pellets had comparable masses of approximately 5 mg. The electrochemical behavior of the electrode materials was characterized based on the CV curves recorded at scan rates of 1 and 100 mV/s and the galvanostatic discharge curves measured in the current density range of 0.2–20 A g^{-1}. The specific capacitance (C), expressed in F g^{-1}, was calculated according to Eq. 1 for the CV measurements and Eq. 2 for the GCD measurements:

$$C = \frac{\int I \mathrm{d}U}{vm\Delta V}, \tag{2}$$

$$C = \frac{It}{vm\Delta V}, \tag{3}$$

where I, v, ΔV, t and m are the current (A), scan rate (mV s^{-1}), applied potential window (V), discharge time (s) and mass of the electroactive material in one electrode (g), respectively.

Results and discussion

Physicochemical properties of Bi_2S_3

The crystalline structure of the as-synthesized Bi_2S_3 samples was determined by XRD. Figure 1 depicts the XRD patterns of Bi_2S_3 obtained in water and the different solvent mixtures. The peak locations at 2 theta of 15.65, 17.55, 22.35, 23.70, 25.20, 27.35, 28.60, 31.80, 33.00, 33.90, 35.60, 39.00, 40.10, 45.60, 46.55, 52.75, 59.20, 62.60, 65.05 and 69.60 correspond to the (200), (120), (220), (101), (310), (130), (211), (221), (410), (311), (240), (041), (430), (440), (501), (312), (640), (152), (721) and (651) planes of the orthorhombic phase of Bi_2S_3, respectively [42]. The sharp peaks prove that high crystallinity Bi_2S_3 is successfully synthesized using the applied process. Furthermore, secondary crystalline phases, such as crystalline bismuth, sulfur or bismuth oxide, are not present, indicating the high purity of the resulting products. These results correspond well with other reports [24] and confirm that a long reaction time and a synthesis temperature above 140 °C lead to high-purity crystalline Bi_2S_3. As follows from the XRD patterns in Fig. 1, Bi_2S_3-BG/W exhibits the highest crystallinity degree among the synthesized sulfides. The crystallite size of Bi_2S_3 was

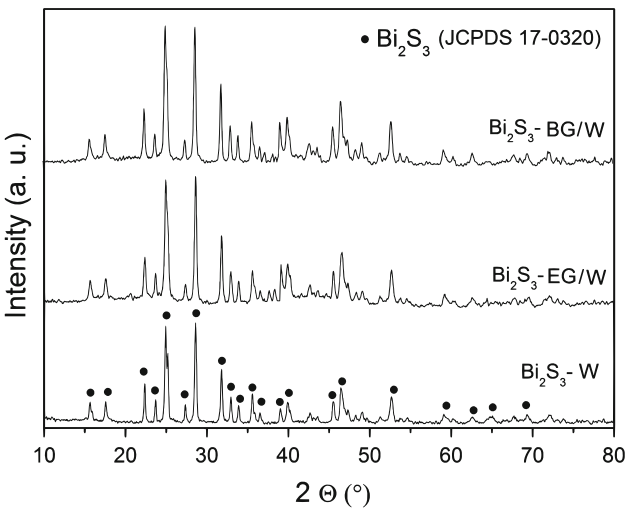

Figure 1 XRD patterns of the Bi_2S_3 samples obtained using different solvent systems.

evaluated for the peak with the highest intensity, recorded at 2 theta of 28.6, using Scherrer's equation. The calculated values were 33, 35 and 39 nm for Bi_2S_3-W, Bi_2S_3-EG/W and Bi_2S_3-BG/W, respectively.

The detailed surface composition of the obtained products was examined by XPS. The XPS survey spectra (Fig. 2a) show signals for only Bi and S, which is consistent with the XRD analysis. The chemical state of Bi_2S_3 was further investigated by high-resolution Bi 4*f* and S 2*p* XPS spectra (Fig. 2b–d). The Bi 4*f* spectrum of Bi_2S_3-W (Fig. 2b) has two predominant peaks at 158.1 and 163.4 eV, which correspond to the spin states of Bi $4f_{7/2}$ and Bi $4f_{5/2}$ in Bi_2S_3. The Bi 4*f* spectra of the other samples show peaks at 158.3 and 163.6 eV for Bi_2S_3-EG/W (Fig. 2c) and 157.7 and 163 eV for Bi_2S_3-BG/W (Fig. 2d). The peak positions in the presented spectra match the energy binding values reported in the literature for Bi^{3+} [34]. Moreover, the nearly symmetric shape of these signals without distinct distortions at their shoulders excludes the presence of metallic Bi and Bi_2O_3, which would appear at 162.4 eV and 157.1 eV [43] and 166 and 161.5 eV [44], respectively. The spin–orbit doublet of S 2*p* overlaps with the Bi 4*f* region. To distinguish between the regions, the magnified core-level S 2*p* spectrum is shown below the Bi 4*f* region for each Bi_2S_3 sample. The S 2*p* region consists of two asymmetric peaks. The signal with a higher intensity located at approximately 162 eV is ascribed to S $2p_{3/2}$. However, the smaller signal at approximately 160.7 eV is attributed to the spin state of S $2p_{1/2}$. The S 2*p* peaks are at 162 and 160.8 eV for Bi_2S_3-W, 161.6 and 160.5 eV for Bi_2S_3-EG/W and 162.2 and 161.1 eV for Bi_2S_3-BG/W. The location of the S $2p_{3/2}$ and S $2p_{1/2}$ signals in the S 2*p* spectra proves that sulfur exists in the S^{2-} valence state in the products [45].

Effect of the solvent mixture on the Bi_2S_3 morphology

The Bi_2S_3 samples were further investigated by FESEM and HRTEM to determine the influence of the solvent on their morphology and microstructure. Figure 3 depicts the representative FESEM images of Bi_2S_3 synthesized in different solvent systems. The solvent is a critical parameter in a solvothermal synthesis that affects the morphology and size of the growing Bi_2S_3 particles. A sphere-like morphology is characteristic of Bi_2S_3-W (Fig. 3a), which forms

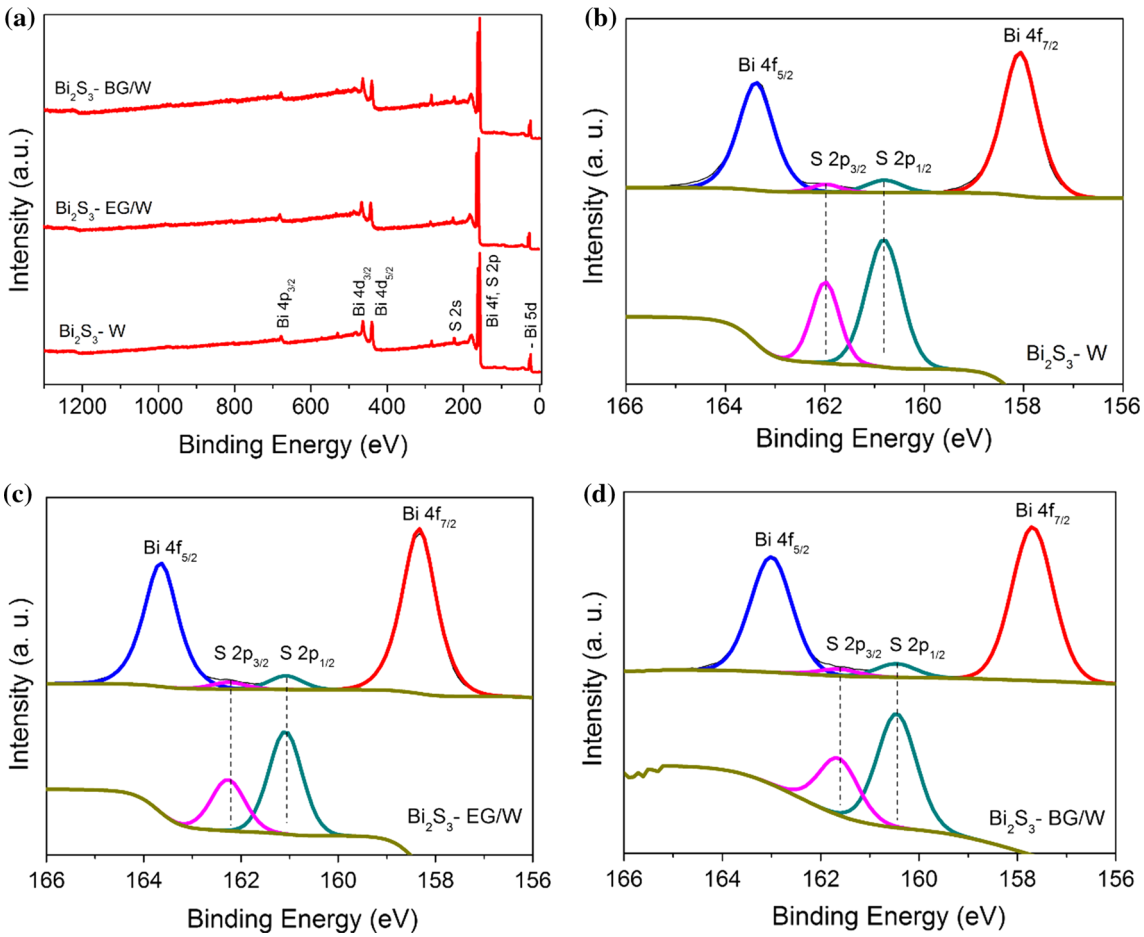

Figure 2 XPS survey (**a**), high-resolution B 4*f* and S 2*p* spectra of Bi_2S_3-W (**b**), Bi_2S_3-EG/W and Bi_2S_3-BG/W (**c**) samples.

aggregates with sizes of 200–300 nm that are composed of clearly distinguishable, small, bean-like particles (Fig. 3b). Highly homogenous and well-separated nanospheres of Bi_2S_3 with sizes in the range of 50–90 nm formed during the synthesis in ethylene glycol/water (Fig. 3c, d). In turn, plate-shaped nanoparticles were observed when the butyldiglycol/water (1:1, v/v) mixture was used (Fig. 3e, f). The HRTEM analysis (Fig. 4) revealed that Bi_2S_3-BG/W is composed of smaller nanorods units 30–50 nm in diameter with 100–200 nm average lengths. The lattice fringe spacings of 0.5041, 0.3672 and 0.5601 nm, which are displayed in the HRTEM images, correspond to the (120) [38], (130) [25] and (200) [38] planes of Bi_2S_3, indicating Bi_2S_3 with different crystalline structures forms under the applied solvothermal conditions.

In most reports on the synthesis of Bi_2S_3, 1D Bi_2S_3 structures, such as nanorods, have been observed [20–22, 25, 28, 30, 34, 38, 44, 46]. The strong tendency of Bi_2S_3 crystals to rapidly and preferential grow along one direction (*c* axis) to form nanorod particles could be a result of the inherent Bi–S chain-type structure [38, 46]. Other reported morphologies of Bi_2S_3 include flowers [24, 27, 29, 32], dandelions [38], nanospheres [37] and microspheres [35], which are three-dimensional architectures composed of nanorod-like particles oriented in different directions. In our study, we demonstrate that the use of a suitable solvent or mixture of solvents enables the formation of nanometer-sized Bi_2S_3 with unique structural forms, including microspheres composed of bean-like units (Bi_2S_3-W) and homogeneous nanospheres (Bi_2S_3-EG/W). Recently, a solvothermal synthesis in a mixed solvent system (including water as a system component) has been shown to be an effective approach for the synthesis of nanostructures with novel shapes and uniform sizes, such as

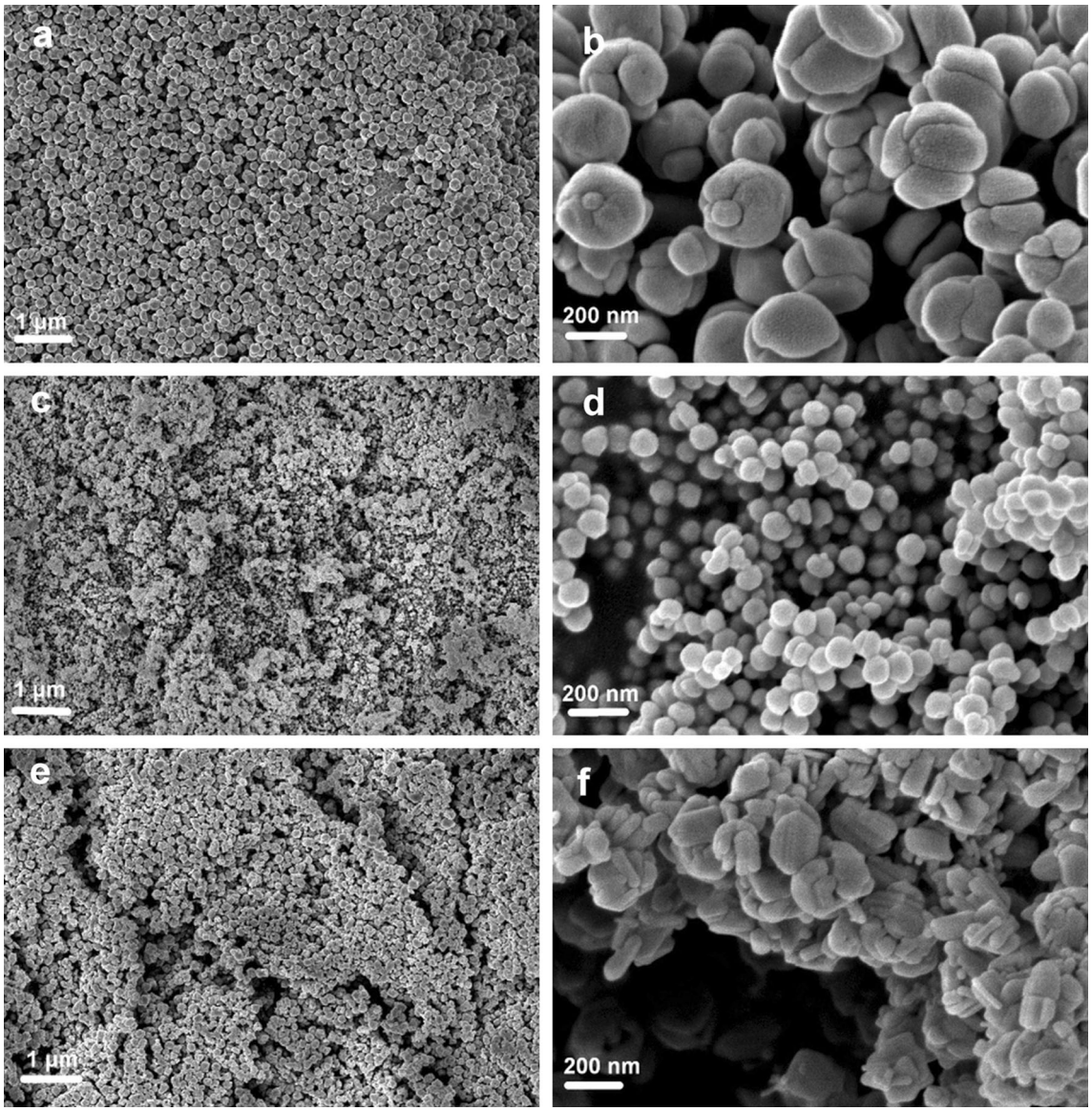

Figure 3 FESEM images of the Bi_2S_3 samples obtained in water (**a**, **b**), ethylene glycol/water (1:1, v/v) (**c**, **d**) and butyldiglycol/water (1:1, v/v) systems (**e**, **f**).

skeleton spheres, cubes, yarn balls and roses [39, 40, 47]. As previously reported [40], adjusting the solvent components and their ratios allows the growth of a metal sulfide with a diverse morphology to be controlled.

The growth of crystal nuclei under solvothermal conditions is determined by the various physical properties of the solvents, including the viscosity, boiling point, surface tension and polarity [36, 37]. The high diffusion rate of ions in a water solution can promote the aggregation [48] of growing Bi_2S_3 nanoparticles, resulting in the formation of spherical aggregates of Bi_2S_3-W. Smaller particles of Bi_2S_3 are obtained when using mixed solvents. Ethylene glycol, which acts as a complexing and capping agent [49], is thought to hinder the favorable anisotropic growth of Bi_2S_3 crystals to yield small spheres with a narrow size distribution (Fig. 3c, d). The butyldiglycol–water system supports the growth of Bi_2S_3 nanorods with relatively small aspect ratios as demonstrated in this study (Fig. 4e, f).

Nitrogen adsorption–desorption isotherms (Fig. A1) were used to determine the textural parameters of Bi_2S_3. According to the Brunauer–Deming–Deming–Teller (BDDT) classification, Bi_2S_3 presents type-IV N_2 sorption isotherms, which are

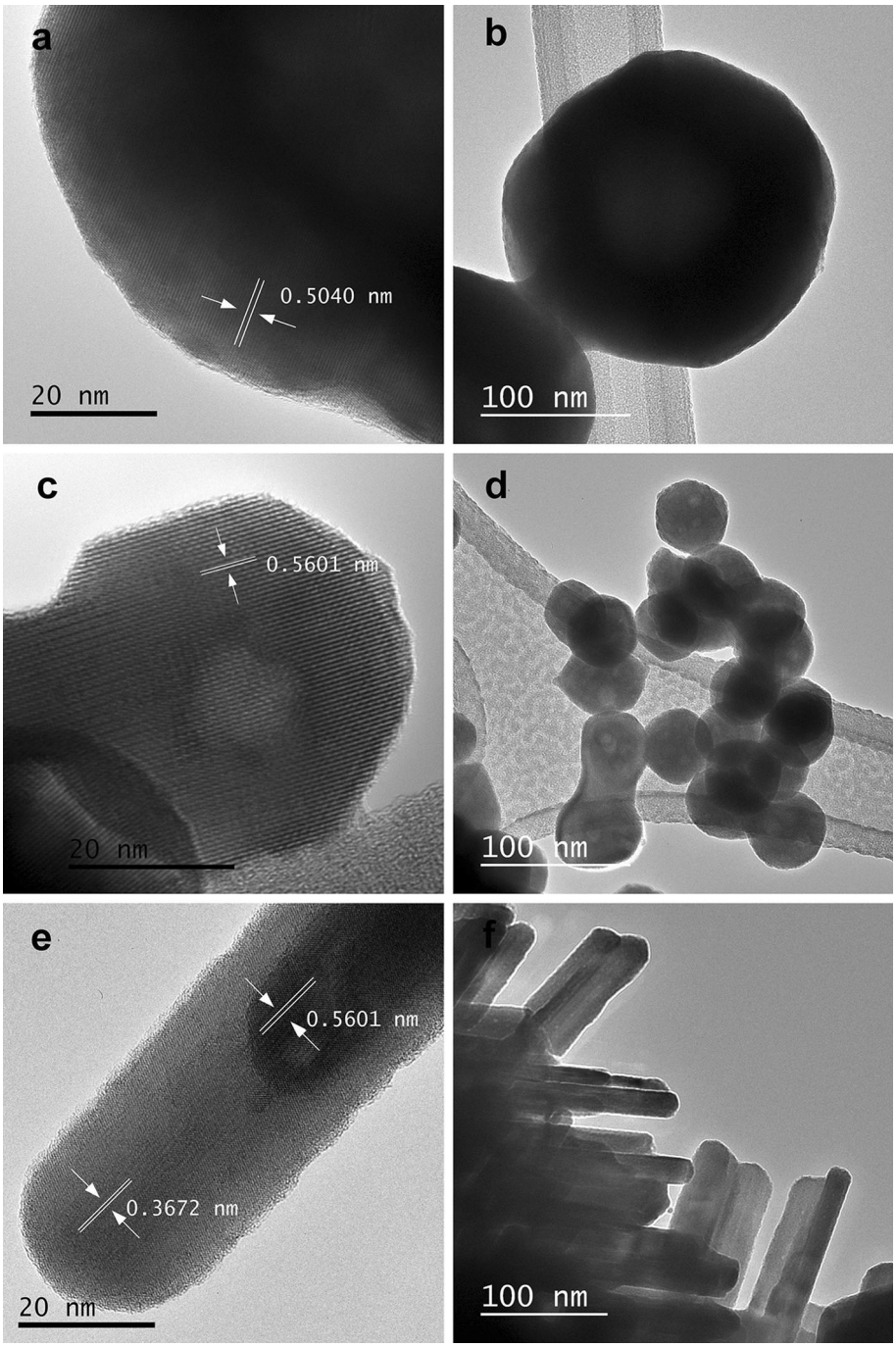

Figure 4 HRTEM images of Bi_2S_3-W (**a**, **b**), Bi_2S_3-EG/W (**c**, **d**) and Bi_2S_3-BG/W (**e**, **f**).

characteristic of mesoporous materials. The calculated textural properties of the samples are given in Table A1. Mesopores contribute 0.88–0.90 of the total pore volume. The Bi_2S_3 samples exhibit BET surface areas in the range of 8–19 $m^2\ g^{-1}$. These S_{BET} values are comparable to those reported for Bi_2S_3 nanoflowers (20 $m^2\ g^{-1}$ [27], 10 $m^2\ g^{-1}$ [29]), Bi_2S_3 nanorods (18 $m^2\ g^{-1}$ [20], 6 $m^2\ g^{-1}$ [22]) and Bi_2S_3 nanobelts (7 $m^2\ g^{-1}$) [41]. Among the synthesized samples, Bi_2S_3-EG/W, which has a nanospherical morphology, demonstrates the highest porosity due to its small nanoparticle size.

Electrochemical measurements of Bi_2S_3

The electrochemical performance of the Bi_2S_3 samples synthesized in different solvent mixtures was determined using CV and GCD measurements. Figure 5

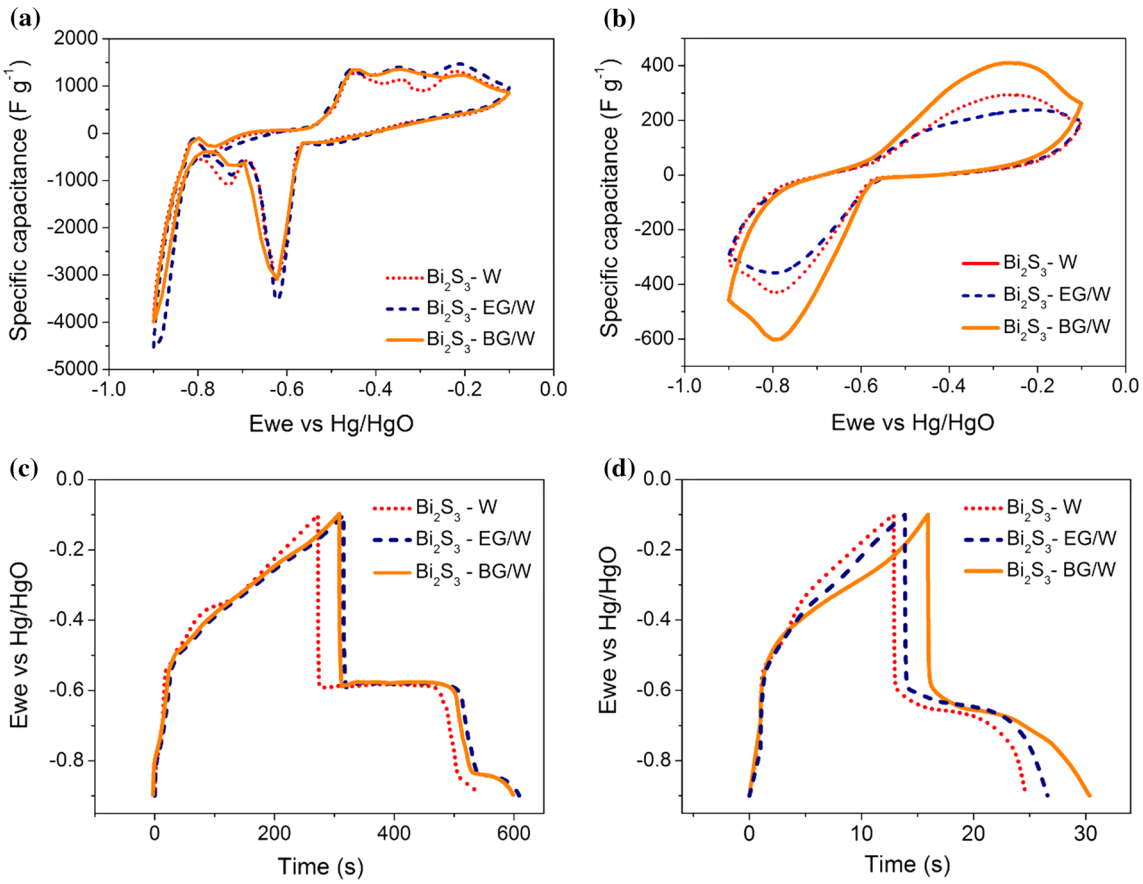

Figure 5 CV curves at 1 mV/s (**a**) and 100 mV/s (**b**), and GCD profiles of the Bi_2S_3 electrodes measured at current densities of 1 A g^{-1} (**c**) and 10 A g^{-1} (**d**) in 6 mol L^{-1} KOH.

shows the typical CV profiles of Bi_2S_3-W, Bi_2S_3-EG/W and Bi_2S_3-BG/W that were recorded at scan rates of 1 mV/s (Fig. 5a) and 100 mV/s (Fig. 5b). As illustrated by the cyclic voltammograms, the tested Bi_2S_3-based electrode materials operate in a wide potential window from − 0.1 to − 0.9 V, resulting in a high current response. The distinct redox peaks ascribed to the pseudocapacitive behavior of Bi_2S_3 appear at − 0.6 and − 0.45 V during the anodic and cathodic sweeps, respectively. The redox couple can arise from the change in the bismuth valence state (Bi^{3+}/Bi^0) [28, 50] or be induced by the frequently reported reversible reaction between Bi_2S_3 and the OH^- ions in the electrolyte ($Bi_2S_3 + OH^- \rightarrow Bi_2S_3$-$OH + H_2O + e^-$) [20]. In our work, the positions of redox peaks in the CV curves perfectly match the potential values for the Bi^{3+}/Bi^0 change in the Bi_2O_3-based electrodes reported in the literature. The other redox peak pairs observed in Fig. 5a could be related to the adsorption–desorption of hydrogen in Bi_2S_3 [23]. However, as the scan rate increases, most of the redox peaks fade, and at 100 mV s^{-1}, only one redox couple, which is attributed to the reversible adsorption of hydrogen, can be distinguished (Fig. 5b). The specific capacitances of Bi_2S_3-W, Bi_2S_3-EG/W and Bi_2S_3-BG/W, as calculated from the CV curves recorded at 1 mV/s, are 608, 630 and 615 F g^{-1}, respectively. However, Bi_2S_3-BG/W, which has a specific capacitance value of 168 F g^{-1} (at 100 mV s^{-1}), demonstrates a superior rate capability compared with that of Bi_2S_3-W (106 F g^{-1}) and Bi_2S_3-EG/W (118 F g^{-1}).

In accordance with the CV results, the GCD discharge curves of the Bi_2S_3 electrodes (Fig. 5c) show two distinct plateaus at − 0.6 V and − 0.85 V indicating the pseudocapacitive nature of the charge storage in Bi_2S_3. Figure 5d shows that the smaller plateau at − 0.85 V disappears at a high current density of 10 A g^{-1} because of diffusion limitations and the resulting insufficient intercalation of the

electrochemically active material with the electrolyte ions at high current densities.

The relationship between the specific capacitance and current density of the Bi_2S_3 electrodes determined based on the GCD measurements is shown in Fig. 6a. Bi_2S_3-EG/W demonstrates the highest specific capacitance of 632 F g^{-1} at 0.5 A g^{-1} compared with that of Bi_2S_3-W (448 F g^{-1}) and Bi_2S_3-BG/W (550 F g^{-1}). The remarkable capacitive behavior of Bi_2S_3-EG/W at low current loading can be ascribed to its high specific surface area, S_{BET} (19 m^2 g^{-1}), which is approximately 1.5–2 times higher than that of the other Bi_2S_3 samples (Table A1) and can provide more electrochemically active sites for the electron transfer reactions. However, the main advantage of Bi_2S_3-BG/W over the other samples is its excellent rate capabilities of 72% and 50% at current densities of 5 A g^{-1} and 10 A g^{-1}, respectively. In comparison, the rate capability for Bi_2S_3-W and Bi_2S_3-EG/W is markedly lower, approximately 65% at 5 A g^{-1}.

In our study, the specific capacitances of the Bi_2S_3 electrodes at 1 A g^{-1} range from 342 to 374 F g^{-1}. These values are significantly higher than those reported by Nie et al. (60 F g^{-1}) [25], Vadivel et al. (191 F g^{-1}) [20], Liu et al. (233 F g^{-1}) [27], Liang et al. (270 F g^{-1}) [22] and Noordeen et al. (152 F g^{-1}) [32] at the same current density.

The resistive properties of the Bi_2S_3 electrodes were evaluated via EIS analysis (Fig. 6b). The impedance spectra consist of a semicircle in the high-frequency region (the inset of Fig. 6b) and a line in the low-frequency range, which correspond to the charge transfer resistance (R_{ct}) and diffusion/transport resistance (R_w) of the ions in the electrolyte, respectively. The remarkable electrochemical performance of the Bi_2S_3-BG/W electrode can be ascribed to its good conductive properties, which are reflected by a very low bulk resistance (R_s) (0.08 Ω). In comparison, the recorded R_s values for Bi_2S_3-W and Bi_2S_3-EG/W are 0.14 and 0.13 Ω, respectively. The nearly vertical line for Bi_2S_3-BG/W in the low-frequency region indicates high ion mobility in the electrolyte and fast adsorption on the electrode surface. Meanwhile, the lower slopes of this curve in the same region, recorded for Bi_2S_3-W and Bi_2S_3-EG/W, can suggest diffusion difficulties of ions into the pores of electrode material [18]. The largest semicircle diameter (R_{ct} = 0.80 Ω) was recorded for Bi_2S_3-EG/W, suggesting the high intrinsic resistance of this electrode material and sluggish redox reaction kinetics, which result in a rate capability worse than that of the Bi_2S_3-W (0.40 Ω) and Bi_2S_3-BG/W (0.63 Ω) electrodes.

These results demonstrate that the Bi_2S_3 morphology affects the conductive and electrochemical properties of the electrode material. The superior charge mobility of the Bi_2S_3-BG/W nanoplates is related to the presence of nanorod-like particles in the sample, and these particles provide short paths for unrestrained electron transport along their axis at high charge/discharge rates [51]. In turn, the electron propagation mechanism in Bi_2S_3 micro- and nanospheres is expected to be more random, i.e., without a preferential direction, resulting in insufficient utilization of the electroactive sites for redox reactions at high current densities. Ramasamy et al. [52] also confirmed the advantage of a nanoplate-like morphology over other morphologies for supercapacitor applications and indicated that a layered nanoplate

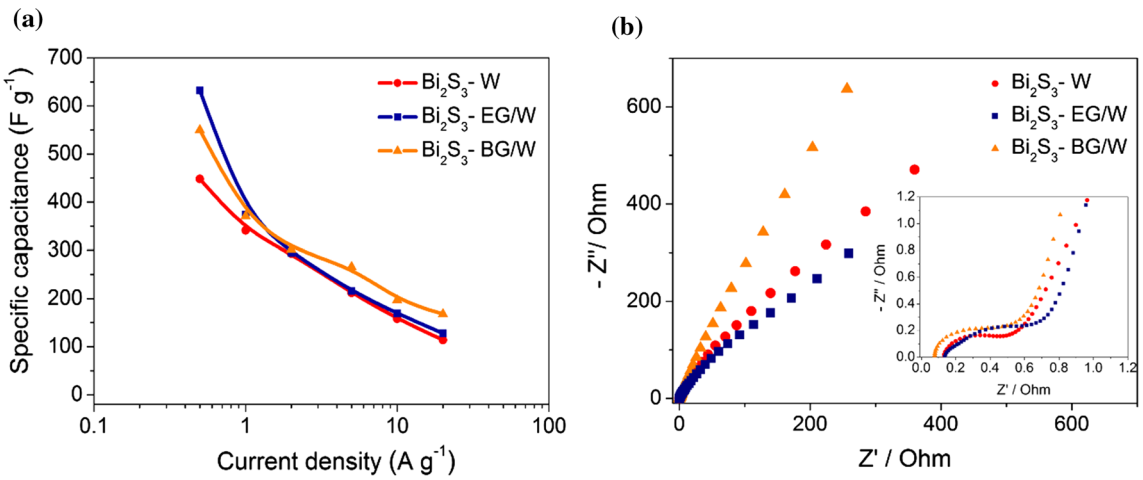

Figure 6 Specific capacitance vs current density (**a**) and Nyquist plots of the tested Bi_2S_3 electrodes (**b**).

structure ensures effective insertion and extraction of electrolyte ions.

The cyclability test of the Bi_2S_3 samples was performed at a current density of 1 A g^{-1} for 500 cycles, as shown in Fig. 7. A remarkable electrochemical stability is obtained for Bi_2S_3-BG/W and Bi_2S_3-W, and they retain 87% and 73% of their initial capacitances, respectively, after the galvanostatic charge/discharge test. The presented cycling performance of the Bi_2S_3 electrodes is comparable to that reported for Bi_2S_3/rGO composites [20, 25]. Distinct variations in the specific capacitance are observed up to the 200th cycle and are followed by a stabilization period (almost a constant capacitance retention) in the samples. This type of behavior has also been reported in previous studies [6, 27]. The above-mentioned capacitance changes can be ascribed to the electrode material adjusting to the mechanical stress induced by the reversible insertion/de-insertion of electrolyte ions into the bulk material [25, 53]. Thus, the improvement in the specific capacitance during cycling could be due to the active surface area for charge storage increasing. The Bi_2S_3-EG/W electrode demonstrates the worst cycling stability among the tested materials, which is reflected by a low capacitance retention of 30% after 500 cycles. This may suggest the strong tendency of the nanosphere-like particles of Bi_2S_3-EG/W to aggregate during the cycling test, leading to significant changes in morphology and decreasing capacitive properties. Moreover, morphology rearrangements during cycling can result in the loss of electroactive material, resulting in the gradual capacitance decline [26].

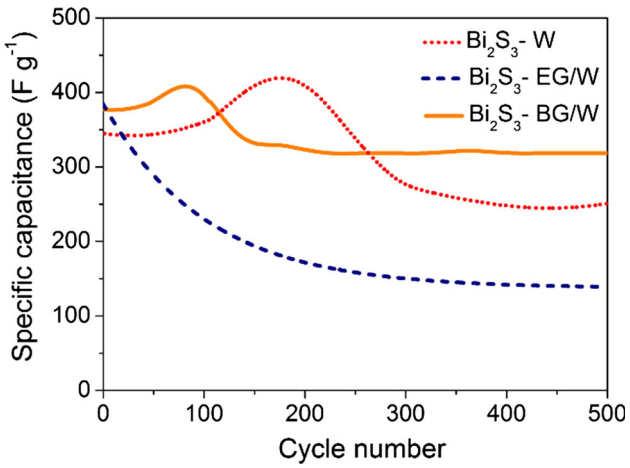

Figure 7 Cycling performances of the Bi_2S_3 electrodes at a current density of 1 A g^{-1} in 6 mol L^{-1} KOH.

Conclusions

In conclusion, the solvent system in a solvothermal approach is a critical parameter that determines the morphology of the obtained Bi_2S_3. The syntheses in water and ethylene glycol/water (1:1, v/v) and butyldiglycol/water (1:1, v/v) mixtures led to the successful formation of very pure sphere-, nanosphere- and nanoplate-like particles of Bi_2S_3, respectively. The as-synthesized Bi_2S_3 samples have different electrochemical behaviors and cycle performances based on their morphologies. Of the samples, Bi_2S_3-BG/W exhibits the best capacitive performance over the whole range of current densities with a high specific capacitance of 550 F g^{-1} at 0.5 A g^{-1}. This sample also has a remarkable rate capability of 72% at a high current density of 5 A g^{-1}, due to the nanorod-like units assembling into nanoplate structures, which favors rapid electron transfer in the electrode material. Furthermore, Bi_2S_3-BG/W demonstrates a very good electrochemical stability with 87% capacitance retention after 500 charge–discharge cycles. This work encourages the future design and engineering of hybrid materials with a graphene material to further improve the performance of Bi_2S_3-based electrodes for supercapacitors.

Acknowledgements

This work was supported by a statutory activity subsidy from the Polish Ministry of Science and Higher Education for the Faculty of Chemistry of Wrocław University of Science and Technology.

Compliance with ethical standards

Conflicts of interest All authors declare that they have no conflict of interest.

Electronic supplementary material: The online version of this article (https://doi.org/10.1007/s10853-018-2785-3) contains supplementary material, which is available to authorized users.

References

[1] Yu G, Xie X, Pan L, Bao Z, Cui Y (2013) Hybrid nanostructured materials for high-performance electrochemical capacitors. Nano Energy 2:213–234

[2] Ho MY, Khiew PS, Isa D, Tan TK (2014) A review of metal oxide composite electrode materials for electrochemical capacitors. NANO 9(6):1430002–1430027

[3] Beguin F, Frąckowiak E (2013) Supercapacitors: materials, systems and applications. Wiley, London

[4] Gu W, Yushin G (2014) Review of nanostructured carbon materials for electrochemical capacitor applications: advantages and limitations of activated carbon, carbide-derived carbon, zeolite-templated carbon, carbon aerogels, carbon nanotubes, onion-like carbon, and graphene. WIREs Energy Environ 3:424–473

[5] Toupin M, Brousse T, Belanger D (2004) Charge storage mechanism of MnO_2 electrode used in aqueous electrochemical capacitor. Chem Mater 16(16):3184–3190

[6] Cheng Q, Tang J, Ma J, Zhang H, Shinya N, Qin LCh (2011) Graphene and nanostructured MnO_2 composite electrodes for supercapacitors. Carbon 49:2917–2925

[7] Miniach E, Śliwak A, Moyseowicz A, Fernandez-Garcia L, Gonzalez Z, Granda M, Menendez R, Gryglewicz G (2017) MnO2/thermally reduced graphene oxide composites for high-voltage asymmetric supercapacitors. Electrochim Acta 240:53–62

[8] Śliwak A, Gryglewicz G (2014) High-voltage asymmetric supercapacitors based on carbon and manganese oxide/oxidized carbon nanofiber composite electrodes. Energy Technol 2:819–824

[9] Xiang D, Liu X, Dong X (2017) A facile synthetic method and electrochemical performances of nickel oxide/carbon fibers composites. J Mater Sci 52(13):7709–7718

[10] Sengottaiyan C, Jayavel R, Bairi P, Shrestha RG, Ariga K, Shrestha LK (2017) Cobalt oxide/reduced graphene oxide composite with enhanced electrochemical supercapacitance performance. Bull Chem Soc Jpn 90(8):955–962

[11] Liu GJ, Fan LQ, Yu FD, Wu JH, Liu L, Qiu ZY, Liu Q (2013) Facile one-step hydrothermal synthesis of reduced graphene oxide/Co_3O_4 composites for supercapacitors. J Mater Sci 48(24):8463–8470

[12] Xie S, Zhang M, Liu P, Wang S, Liu S, Feng H, Zheng H, Cheng F (2017) Advanced negative electrode of Fe_2O_3/graphene oxide paper for high energy supercapacitors. Mater Res Bull 96:413–418

[13] Moyseowicz A, Śliwak A, Miniach E, Gryglewicz G (2017) Polypyrrole/iron oxide/reduced graphene oxide ternary composite as a binderless electrode material with high cyclic stability for supercapacitors. Compos Part B Eng 109:23–29

[14] Qi T, Jiang J, Chen H, Wan H, Miao L, Zhang L (2013) Synergistic effect of Fe_3O_4/reduced graphene oxide nanocomposites for supercapacitors with good cycling life. Electrochim Acta 114:674–680

[15] Wang Y, Song Y, Xia Y (2016) Electrochemical capacitors: mechanism, materials, systems, characterization and applications. Chem Soc Rev 45:5925–5950

[16] Rui X, Tan H, Yan Q (2014) Nanostructured metal sulfides for energy storage. Nanoscale 6:9889–9924

[17] He W, Wang C, Li H, Deng X, Xu X, Zhai T (2017) Ultrathin and porous Ni_3S_2/$CoNi_2S_4$ 3D-network structure for superhigh energy density asymmetric supercapacitors. Adv Energy Mater 7(21):1700983

[18] He W, Liang Z, Ji K, Sun Q, Zhai T, Xu X (2018) Hierarchical Ni–Co–S@Ni–W–O core-shell nanosheet arrays on nickel foam for high-performance asymmetric supercapacitors. Nano Res 11(3):1415–1425

[19] Pineda E, Nicho ME, Nair PK, Hu H (2012) Optoelectronic properties of chemically deposited Bi_2S_3 thin films and the photovoltaic performance of Bi_2S_3/P3OT solar cells. Sol Energy 86(4):1017–1022

[20] Vadivel S, Nirmalesh Naveen A, Kamalakannan VP, Cao P, Balasubramanian N (2015) Facile large scale synthesis of Bi_2S_3 nanorods-graphene composite for photocatalytic photoelectrochemical and supercapacitor application. Appl Surf Sci 351:635–645

[21] Ma L, Zhao Q, Zhang Q, Ding M, Huang J, Liu X, Liu Y, Wu X, Xu X (2014) Controlled assembly of Bi_2S_3 architectures as Schottky diode, supercapacitor electrodes and highly efficient photocataysts. RSC Adv 4:41636–41641

[22] Liang K, Wang C, Xu X, Leng J, Ma H (2017) Capacitive and photocatalytic performance of Bi_2S_3 nanostructures synthesized by solvothermal method. Phys Lett A 381:652–657

[23] Hu P, Cao Y, Lu B (2013) Flowerlike assemblies of Bi_2S_3 nanorods by solvothermal route and their electrochemical hydrogen storage performance. Mater Lett 106:297–300

[24] Zhang M, Chen DJ, Wang RZ, Feng JJ, Bai Z, Wang AJ (2013) D-penicillamine assisted hydrothermal synthesis of Bi_2S_3 nanoflowers and their electrochemical application. Mater Sci Eng C 33:3980–3985

[25] Nie G, Lu X, Lei J, Yang L, Wang C (2015) Facile and controlled synthesis of bismuth sulfide nanorods-reduced

graphene oxide composites with enhanced supercapacitor performance. Electrochim Acta 154:24–30

[26] Tang Y, Chen T, Yu S, Qiao Y, Mu S, Hu J, Gao F (2015) Synthesis of graphene oxide anchored porous manganese sulfide nanocrystals via the nanoscale Kirkendall effect for supercapacitors. J Mater Chem A 3:12913–12919

[27] Liu KL, Chen F, Liu Y, Li D, Shi WD (2017) Synthesis of hierarchal Bi_2S_3 nanoflowers via a topotactic transformation from hierarchal Bi_2WO_6 nanoflowers and their supercapacitor performance. Cryst Eng Commun 19:570–575

[28] Yang H, Xie J, Li CM (2014) Bi_2S_3 nanorods modified with $Co(OH)_2$ ultrathin nanosheets to significantly improve its pseudocapacitance for high specific capacitance. RSC Adv 4:48666–48670

[29] Mukkabla R, Deepa M, Srivastava AK (2015) Poly(3,4-ethylenedioxypyrrole) enwrapped Bi_2S_3 nanoflowers for rigid and flexible supercapacitors. Electrochim Acta 164:171–181

[30] Liu F, Shao X, Li H, Wang M, Yang S (2013) Facile fabrication of Bi_2S_3-ZnS nanohybrids on graphene sheets with enhanced electrochemical performances. Mater Lett 108:125–128

[31] Raut SS, Dhobale JA, Sankapal BR (2017) SILAR deposited Bi_2S_3 thin film towards electrochemical supercapacitor. Phys E Low Dimens Syst Nanostruct 87:209–212

[32] Noordeen AK, Sambasivam S, Chinnasamy S, Ramasamy J, Subramani T (2018) Hierarchical flower structured Bi_2S_3/reduced graphene oxide nanocomposite for high electrochemical performance. J Inorg Organomet Polym 28:73–83

[33] Lu H, Guo Q, Zan F, Xia H (2017) Bi_2S_3 nanoparticles anchored on graphene nanosheets with superior electrochemical performance for supercapacitors. Mater Res Bull 96:471–477

[34] Lou W, Chen M, Wang X, Liu W (2007) Novel single-source precursors approach to prepare highly uniform Bi_2S_3 and Sb_2S_3 nanorods via a solvothermal treatment. Chem Mater 19:872–878

[35] Zhou X, Zhao X, Zhang D, Chen S, Guo X, Deng W, Chen Y (2006) Hollow microscale organization of Bi_2S_3 nanorods. Nanotechnology 17:3806–3811

[36] Xiang W, Yang Y, Yang J, Yuan H, An J, Wei J, Liu X (2014) Surfactant and thioacetamide—assisted reflux synthesis of Bi_2S_3 nanowires. J Mater Res 29(19):2272–2287

[37] Ma L, Wu J, Wang S, Yang H, Liang D, Lu Z (2017) Synergistic antibacterial effect of Bi_2S_3 nanospheres combined with ineffective antibiotic gentamicin against methicillin-resistant Staphylococcus aureus. J Inorg Biochem 168:38–45

[38] Tian L, Tan HY, Vittal JJ (2008) Morphology-controlled synthesis of Bi_2S_3 nanomaterials via single- and multiple-source approaches. Cryst Growth Des 8(2):734–738

[39] Liu Z, Liang J, Peng S, Qian Y (2004) Synthesis and growth mechanism of Bi_2S_3 nanoribbons. Chem Eur J 10:634–640

[40] Dong W, Wang X, Li B, Wang L, Chen B, Li C, Li X, Zhang T, Shi Z (2011) Hydrothermal synthesis and structure evolution of hierarchical cobalt sulfide nanostructures. Dalton Trans 40:243–248

[41] Xing R, Li D, An C, Zhang L, Li Q, Liu S (2012) Single-crystalline Bi_2S_3 nanobelts: hydrothermal synthesis and growth mechanism. J Nanosci Nanotechnol 12:8029–8033

[42] Dutta AK, Maji SK, Mitra K, Sarkar A, Saha N, Ghosh AB, Adhikary B (2014) Single source precursor approach to the synthesis of Bi_2S_3 nanoparticles: a new amperometric hydrogen peroxide biosensor. Sens Actuator B Chem 192:578–585

[43] Escobar-Alarcon L, Morales-Mendez JG, Solis-Casados DA, Romero S, Fernandez M, Haro-Poniatowski E (2015) Preparation and characterization of bismuth nanostructures deposited by pulsed laser ablation. J Phys Conf Ser 582:012013

[44] Thomson JW, Cademartiri L, MacDonald M, Petrov S, Calestani G, Zhang P, Ozin GA (2010) Ultrathin Bi_2S_3 nanowires: surface and core structure at the cluster-nanocrystal transition. J Am Chem Soc 132:9058–9068

[45] Grigas J, Talik E, Lazauskas V (2002) X-ray Photoelectron Spectra and electronic structure of Bi_2S_3 crystals Phys. Stat Sol 232(2):220–230

[46] Zhu JM, Yang K, Zhu JJ, Ma GB, Zhu XH, Zhou SH, Liu ZG (2003) The microstructure studies of bismuth sulfide nanorods prepared by sonochemical method. Opt Mater 23:89–92

[47] Jiang Y, Xie B, Wu J, Yuan S, Wu Y, Haung H, Qian Y (2002) Room temperature synthesis of copper and silver, nanocrystalline chalcogenides in mixed solvents. J Solid State Chem 167:28–33

[48] Peng H, Ma G, Mu J, Sun K, Lei Z (2014) Controllable synthesis of CuS with hierarchical structures via a surfactant-free method for high-performance supercapacitors. Mater Lett 122:25–28

[49] Shambharkar BN, Chowdhury AP (2016) Ethylene glycol mediated synthesis of Ag_8SnS_6 nanoparticles and their exploitation in the degradation of eosin yellow and brilliant green. RSC Adv 6:10513–10519

[50] Ng CH, Lim HN, Hayase S, Zainal Z, Shafie S, Huang NM (2018) Effects of temperature on electrochemical properties of bismuth oxide/manganese oxide pseudocapacitor. Ind Eng Chem Res 57:2146–2154

[51] Liu X, Zhang Y, Zhang X, Xia Z, Wang H, Sun J, Dong R, Wang F (2015) Crystallographically-oriented Mn oxide nanorod/nanowire arrays electrodes. J Alloys Compd 620:390–398

[52] Ramasamy K, Gupta RK, Sims H, Palchoudhury S, Ivanov S, Gupta A (2015) Layered ternary sulfide $CuSbS_2$ nanoplates for flexible solid-state supercapacitors. J Mater Chem A 3:13263–13274

[53] Reddy RN, Reddy RG (2006) Porous structured vanadium oxide electrode material for electrochemical capacitors. J Power Sources 156(2):700–704